



Transversely Isotropic Poroelastic Behaviour of the Callovo-Oxfordian Claystone: A Set of Stress-Dependent Parameters

Philipp Braun¹ · Siavash Ghabezloo¹ · Pierre Delage¹ · Jean Sulem¹ · Nathalie Conil²

Received: 5 May 2019 / Accepted: 5 October 2020 / Published online: 21 October 2020
© Springer-Verlag GmbH Austria, part of Springer Nature 2020

Abstract

In the framework of a deep geological radioactive waste disposal in France, the hydromechanical properties of the designated host rock, the Callovo-Oxfordian claystone (COx), are investigated in laboratory tests. Experiments presented in this study are carried out to determine several coefficients required within a transversely isotropic material model. They include isotropic compression tests, pore pressure tests, and deviatoric loading tests parallel and perpendicular to the bedding plane. We emphasize the adapted experimental devices and testing procedures, necessary to detect small strains under high pressures, on a material, which is sensitive to water and has a very low permeability. In particular, we discovered a significant decrease of elastic stiffness with decreasing effective stress, which was observed to be reversible. In both isotropic and deviatoric tests, a notable anisotropic strain response was found. The Young modulus parallel to bedding was about 1.8 times higher than the one perpendicular to the bedding plane. A notably low Poisson ratio perpendicular to the bedding plane with values between 0.1 and 0.2 was evidenced. While the anisotropy of the back-calculated Biot coefficient was found to be low, a significant anisotropy of the Skempton's coefficient was computed. The performed experiments provide an overdetermined set of material parameters at different stress levels. Using all determined parameters in a least square error regression scheme, seven independent elastic coefficients and their effective stress dependency are characterized. Parameters measured under isotropic loading are well represented by this set of coefficients, while the poroelastic framework with isotropic stress dependency is not sufficient to describe laboratory findings from triaxial loading.

Keywords Claystone · Transverse isotropy · Triaxial testing · Stress dependency · Poroelasticity

List of Symbols

ε_i	Strain vector containing the six independent components of the second rank strain tensor	ν'_{zh}	Apparent drained Poisson's ratio under loading parallel to bedding
M_{ij}	Drained stiffness tensor in matrix format	ν_{hh}	Drained Poisson's ratio parallel to bedding
C_{ij}	Drained compliance tensor in matrix format	G	Shear modulus perpendicular to bedding
σ_i	Stress vector containing the six independent components of the second rank stress tensor	G'	Shear modulus parallel to bedding
b_i	Biot's coefficient for i -th direction	ϕ_0	Porosity
p_f	Pore fluid pressure	M	Biot's undrained modulus M
E_i	Drained Young's modulus in the i -th direction	N	Biot's skeleton modulus N
ν_{zh}	Drained Poisson's ratio perpendicular to bedding	K_f	Bulk modulus of the pore fluid
		K_ϕ	Unjacketed pore modulus
		B_i	Skempton's coefficient for i -th direction
		K_s	Unjacketed bulk modulus
		M_{ij}^u	Undrained stiffness tensor in matrix format
		C_{ij}^u	Undrained compliance tensor in matrix format
		$E_{u,i}$	Undrained Young's modulus in the i -th direction
		$\nu_{u,zh}$	Undrained Poisson's ratio perpendicular to bedding
		$\nu_{u,hh}$	Undrained Poisson's ratio parallel to bedding
		σ'	Terzaghi isotropic effective stress

✉ Philipp Braun
philipp.braun@enpc.fr

¹ Laboratoire Navier, 6-8 Avenue Blaise-Pascal, Cité Descartes 77455 Champs-sur-Marne, Paris, France

² Andra, Meuse/Haute-Marne Underground Research Laboratory, Bure, France

σ	Isotropic total stress
ε_v	Volumetric strain
K_d	Isotropic drained bulk modulus
H	Biot's pore pressure loading modulus
b	Isotropic Biot's coefficient
V	Specimen volume
m_f	Pore fluid mass
K_u	Isotropic undrained bulk modulus
B	Isotropic Skempton's coefficient
D_i	Drained isotropic compression modulus in the i -th direction
U_i	Undrained isotropic compression modulus in the i -th direction
H_i	Biot's pore pressure loading modulus in the i -th direction
R_D	Anisotropy ratio in drained isotropic compression
R_U	Anisotropy ratio in undrained isotropic compression
R_H	Anisotropy ratio in pore pressure loading
R_E	Anisotropy ratio of drained Young's moduli
q	Deviatoric stress
E_z^∞, E_z^0, β	Model parameters for regression analysis
ρ	Wet density
ρ_d	Dry density
w	Water content
S_r	Saturation degree
s	Suction
S	Standard deviation of the estimate

1 Introduction

The French National Agency for Nuclear Waste Management, Andra, is investigating the possibility of constructing a deep geological nuclear waste disposal facility in the Callovo-Oxfordian (COx) claystone, located in the east of France.

To study the host material and demonstrate the feasibility of the project, Andra constructed an underground research laboratory (URL) at 490 m depth, where the claystone has an average porosity of 17.5 % and an average water content of 7.9 % (Conil et al. 2018). An average clay content around 42 % was mentioned by the same authors. Wileveau et al. (2007) determined a vertical and a minor horizontal total stress close to 12 MPa, a major horizontal stress close to 16 MPa and a pore pressure of 4.9 MPa.

During extensive laboratory studies on its hydro-mechanical behaviour, the COx claystone was found transversely isotropic with larger stiffness parallel to the bedding plane (Chiarelli 2000; Escoffier 2002; Andra 2005; Mohajerani et al. 2012; Zhang et al. 2012; Belmokhtar et al. 2017b). This feature, revealed also in many other types of shales, can

be attributed to the sedimentary history of the material. Due to this fact, transversely isotropic poroelasticity was chosen as a framework for hydromechanical modelling purposes. A larger number of experiments is therefore necessary, compared to an isotropic material, to capture the complete material behaviour (e.g. two triaxial tests have to be carried out to determine the Young moduli and Poisson ratios both perpendicular and parallel to the bedding plane). While there are extensive data on the Young moduli perpendicular to bedding, provided by the aforementioned authors, fewer data are given on the Young modulus parallel to bedding and the Poisson ratios of saturated COx (Menaceur et al. 2015; Belmokhtar et al. 2018). Several experiments for establishing a set of poroelastic parameters were carried out in the present work. This includes triaxial compression parallel and perpendicular to the bedding plane in drained and undrained conditions, isotropic compression tests in both drained and undrained conditions, and pore pressure loading tests under constant total stress. The anisotropic strain response was measured in all experiments.

The COx claystone can be considered as a swelling claystone (Schmitt et al. 1994). In its natural state, the claystone is fully saturated. Therefore, swelling can only be induced when the material is brought in contact with water after desaturation, or when it is submitted to an effective stress release. Several authors working on this rock reported an increase of stiffness and mechanical resistance with decreasing water content. Even though specimens are well protected from drying during all handling phases from core extraction to laboratory testing, they desaturate slightly, with a saturation degree between 90 and 95 % generally observed. To evaluate parameters on specimens under well-defined saturated conditions, the specimens have to be hydrated in the testing apparatus. Special attention was paid here, as the application of stress during this phase is indispensable for avoiding free swelling and limiting specimen damage. Due to the low permeability of the claystone, the saturation time might become very long, which is why we used adapted testing devices, allowing us to reduce the drainage length of the specimens to 10 mm (Tang et al. 2008; Belmokhtar et al. 2017b, 2018). Improved testing procedures, presented in detail by Braun et al. (2019) were followed, comprised of step loading, which enable a better distinction between drained and undrained specimen state in the experiments. These time efficient procedures permit us to evaluate several poroelastic coefficients in each loading step, and hence to analyse inter-compatible parameters as a function of the isotropic effective stress.

We refer here also to our companion paper (Braun et al. 2020), in which we investigated the thermal properties of the COx claystone under constant stress conditions. The present work was carried out under isothermal conditions, without any influence of thermal effects. However, in the companion

paper we discuss thermal characteristics in undrained conditions, which are strongly coupled with the hydromechanical properties described in the following.

2 Poro-Elastic Framework

In this work, we analyse the mechanical response of a porous rock due to external stress and pore pressure loading, based on the poroelastic constitutive equations, first described by Biot and Willis (1957). For a transversely isotropic material one finds identical parameters for both directions $x = y = h$ parallel to the bedding plane and different properties in the direction z (perpendicular to the bedding plane). The transversely isotropic poroelastic stress-strain relationship can be written as (Cheng 1997):

$$d\sigma_i = M_{ij}d\epsilon_j + b_i dp_f \tag{1}$$

where σ_i and ϵ_i denote the stress and strain tensors, respectively, M_{ij} the stiffness matrix, b_i the Biot coefficients in the i direction and p_f the pore fluid pressure. The strain tensor σ_i is composed of:

$$\sigma_i = [\sigma_x, \sigma_y, \sigma_z, \sigma_{xy}, \sigma_{yz}, \sigma_{zx}]^T \tag{2}$$

The planes and directions in which the different stress tensor components and the material properties intervene is schematically represented in Fig. 1. The strains in different directions are contained within the strain vector ϵ_i :

$$\epsilon_i = [\epsilon_x, \epsilon_y, \epsilon_z, \epsilon_{xy}, \epsilon_{yz}, \epsilon_{zx}]^T \tag{3}$$

The vector b_i represents the Biot effective stress coefficients in both directions of anisotropy:

$$b_i = [b_h, b_h, b_z, 0, 0, 0]^T \tag{4}$$

We can also write the stiffness matrix M_{ij} as follows:

$$M_{ij} = \begin{pmatrix} M_{11} & M_{12} & M_{13} & 0 & 0 & 0 \\ M_{12} & M_{11} & M_{13} & 0 & 0 & 0 \\ M_{13} & M_{13} & M_{33} & 0 & 0 & 0 \\ 0 & 0 & 0 & 2G' & 0 & 0 \\ 0 & 0 & 0 & 0 & 2G & 0 \\ 0 & 0 & 0 & 0 & 0 & 2G \end{pmatrix} \tag{5}$$

$$M_{11} = \frac{E_h(E_z - E_h\nu_{zh}^2)}{(1 + \nu_{hh})(E_z - E_z\nu_{hh} - 2E_h\nu_{zh}^2)} \tag{6}$$

$$M_{12} = \frac{E_h(E_z\nu_{hh} + E_h\nu_{zh}^2)}{(1 + \nu_{hh})(E_z - E_z\nu_{hh} - 2E_h\nu_{zh}^2)} \tag{7}$$

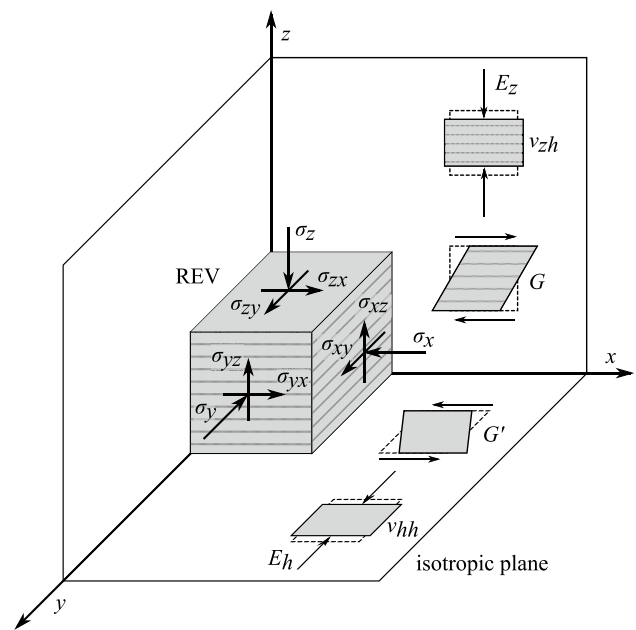


Fig. 1 Representative elementary volume in a transversely isotropic frame, adopted from Popov et al. (2019). The $x - y$ plane corresponds to the isotropic plane. The z axis is oriented perpendicularly to the isotropic plane. Different material properties E_i, ν_i, G and G' describe the material response within the material planes, where the parameters in the $y - z$ plane (not displayed here) are equal to the ones in the $z - x$ plane

$$M_{13} = \frac{E_h E_z \nu_{zh}}{E_z - E_z \nu_{hh} - 2E_h \nu_{zh}^2} \tag{8}$$

$$M_{33} = \frac{E_z^2 (1 - \nu_{hh})}{E_z - E_z \nu_{hh} - 2E_h \nu_{zh}^2} \tag{9}$$

$$G' = \frac{M_{11} - M_{12}}{2} \tag{10}$$

where E_z and ν_{zh} are the Young modulus and the Poisson ratio perpendicular to the bedding plane, and E_h and ν_{hh} parallel to the bedding plane, respectively. G denotes the shear modulus perpendicular to bedding and G' the shear modulus parallel to bedding.

By using the inverse of the stiffness matrix $M_{ij}^{-1} = C_{ij}$, denoted as the drained compliance matrix, one can write:

$$d\epsilon_j = C_{ij}d\sigma_i - C_{ij}b_i dp_f \tag{11}$$

The compliance matrix C_{ij} is written as:

$$C_{ij} = \begin{pmatrix} C_{11} & C_{12} & C_{13} & 0 & 0 & 0 \\ C_{12} & C_{11} & C_{13} & 0 & 0 & 0 \\ C_{13} & C_{13} & C_{33} & 0 & 0 & 0 \\ 0 & 0 & 0 & 1/(2G') & 0 & 0 \\ 0 & 0 & 0 & 0 & 1/(2G) & 0 \\ 0 & 0 & 0 & 0 & 0 & 1/(2G) \end{pmatrix} \quad (12)$$

with

$$\begin{aligned} C_{11} &= 1/E_h \\ C_{12} &= -\nu_{hh}/E_h \\ C_{13} &= -\nu_{zh}/E_z \\ C_{33} &= 1/E_z \\ G' &= E_h/(1 + \nu_{hh}) \end{aligned} \quad (13)$$

In laboratory experiments, the Young moduli and Poisson ratios are generally measured in a triaxial cell under deviatoric loads. The properties E_z and ν_{zh} are determined on a specimen which is submitted to a deviatoric load perpendicular to the bedding plane σ_z , generating strains ϵ_z and

$$\frac{1}{M} = 2(1 - b_h) \left[\frac{(1 - \nu_{hh})b_h}{E_h} - \frac{\nu_{zh}b_z}{E_z} \right] + \frac{(1 - b_z)}{E_z} (b_z - 2\nu_{zh}b_h) + \phi_0 \left(\frac{1}{K_f} - \frac{1}{K_\phi} \right) \quad (15)$$

$\epsilon_x = \epsilon_y$ (Fig. 2). We can then measure $E_z = d\sigma_z/d\epsilon_z$ and $\nu_{zh} = -d\epsilon_x/d\epsilon_z$. A specimen, which is loaded in the direction parallel to the bedding plane (e.g. in direction of y) is required for the remaining properties. Here one is able to observe an axial strain ϵ_y and two different radial strains ϵ_x and ϵ_z . This provides $E_h = d\sigma_y/d\epsilon_y$, $\nu_{hh} = -d\epsilon_x/d\epsilon_y$. The measured parameter $\nu'_{zh} = -d\epsilon_z/d\epsilon_y$ allows us to evaluate of $\nu_{zh} = \nu'_{zh}E_z/E_h$. To be able to determine the shear modulus G perpendicular to the isotropic plane, a third triaxial test is required, where a deviatoric load inclined with respect to the

bedding plane is applied. Such loading would result in shear stresses perpendicular to the bedding plane, mobilizing G , but also inducing inhomogeneous stress and strain distributions within a specimen, which have to be considered in the analysis. While the shear modulus G' is related to the other elastic coefficients (Eq. (10)), G is an independent parameter. The evaluation of G was not carried out in this work and is not further discussed here.

The porosity variation $d\phi$ is given by:

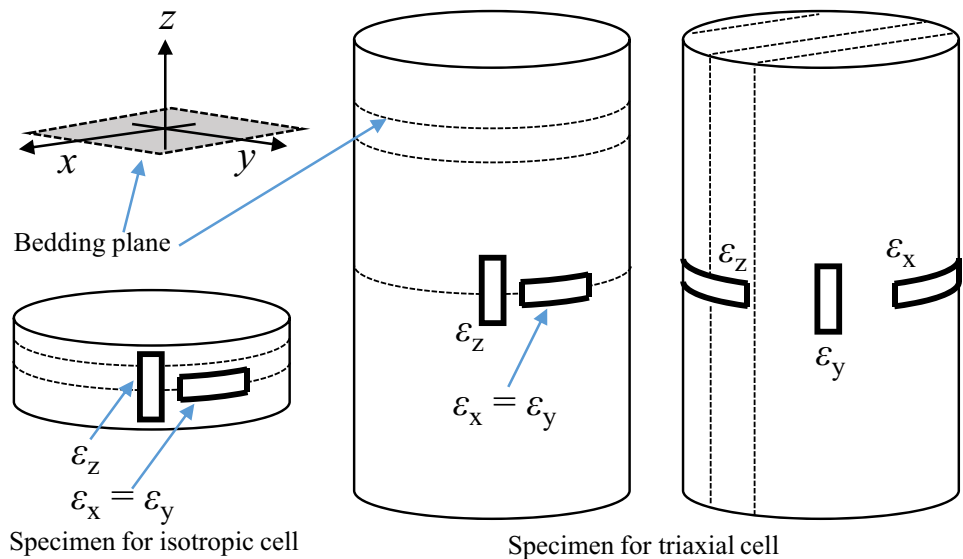
$$d\phi = -b_i d\epsilon_i + \frac{1}{N} dp_f, \quad \frac{1}{N} = \frac{1}{M} - \frac{\phi_0}{K_f} \quad (14)$$

where M is Biot's undrained modulus, N Biot's skeleton modulus and K_f the pore fluid bulk modulus. Note that the expression of porosity variation needs an additional poroelastic parameter with respect to the ones presented previously for the stress-strain relation. The Biot modulus M can be expressed according to Aichi and Tokunaga (2012) by:

with K_ϕ representing theunjacketed pore modulus (Brown and Korringa 1975). In undrained conditions, the fluid mass remains constant and we can write $dm_f = d(\rho_f \phi_0) = 0$. Together with $d\rho_f/\rho_f = dp_f/K_f$ and Eq. (14), we obtain an expression for the pore pressure change in undrained conditions:

$$dp_f = Mb_i d\epsilon_i \quad (16)$$

Fig. 2 Strain gages, oriented and attached with respect to the bedding plane of the COX specimens



Using Eq. (1), one can express the pore pressure change dp_f (Eq. (16)) as a function of total stress change:

$$dp_f = \frac{1}{3} B_i d\sigma_i \tag{17}$$

where:

$$B_i = \frac{3b_j C_{ij}}{\frac{1}{M} + b_i C_{ij} b_j} \tag{18}$$

B_i comprises the anisotropic components of the Skempton's coefficient:

$$B_i = [B_h, B_h, B_z, 0, 0, 0]^T \tag{19}$$

B_z is the Skempton's coefficient parallel to bedding and B_h the Skempton's coefficient perpendicular to bedding, arising from the mathematical framework of transverse isotropy. The classical parameter B used for isotropic materials can here only describe the change of pore pressure under isotropic loading, for which $B = \sum B_i/3$. Under deviatoric loading however, the loading direction influences the amount of generated pore pressure, due to the anisotropic characteristics. Imagine a material with B_z higher than B_h . According to Eq. (17), if this material is loaded in the z direction, it generates a higher pore pressure increase than when loaded by the same amount in the h direction.

Analogously to the drained stiffness matrix, one can determine the undrained stiffness matrix M_{ij}^u with (Cheng 1997):

$$M_{ij}^u = M_{ij} + M b_i b_j \tag{20}$$

The inverse of the undrained stiffness matrix is the undrained compliance matrix C_{ij}^u , which provides the undrained Young's moduli $E_{u,i}$ and the undrained Poisson's ratios $\nu_{u,i}$:

$$\begin{aligned} C_{11}^u &= 1/E_{u,h} \\ C_{12}^u &= -\nu_{u,hh}/E_{u,h} \\ C_{13}^u &= -\nu_{u,zh}/E_{u,z} \\ C_{33}^u &= 1/E_{u,z} \end{aligned} \tag{21}$$

For this transversely isotropic relationship under micro-heterogeneity and micro-isotropy assumptions, seven material coefficients (i.e. $E_h, E_z, \nu_{hh}, \nu_{zh}, b_h, b_z, G$) describe the stress strain relationship, while three additional parameters (K_ϕ, ϕ_0, K_f) are required for the porosity change (Aichi and Tokunaga 2012).

2.1 Isotropic Stress Conditions

When analysing experiments under isotropic stress conditions, it can be helpful to utilize some poromechanical relationships between volume changes and transversely

isotropic deformations. Note that due to the anisotropic framework, the bulk parameters discussed in this section are unable to describe a volume change under mean stress changes in general. Contrary to an isotropic material framework, the parameters can here only be related to isotropic stress changes. Nevertheless, data from isotropic tests can provide complementary information to data from deviatoric stress tests, useful for inferring the complete set of elastic properties.

Under isothermal conditions and isotropic stresses, the volumetric strain ϵ_v is described with respect to the changes in isotropic Terzaghi effective stress $\sigma' = \sigma - p_f$ (where σ is the total confining stress and p_f the pore fluid pressure) as a sum of partial derivatives:

$$d\epsilon_v = \sum d\epsilon_i = \frac{1}{K_d} d\sigma' + \frac{1}{K_s} dp_f \tag{22}$$

in which K_d is the isotropic drained bulk modulus and K_s the unjacketed bulk modulus (Gassmann 1951; Brown and Korrington 1975). We are able to measure the Biot modulus H through a change of pore pressure under constant confining stress, defined as:

$$\frac{1}{H} = \frac{1}{V_0} \left(\frac{\partial V}{\partial p_f} \right)_\sigma = \frac{1}{K_d} - \frac{1}{K_s} \tag{23}$$

The isotropic Biot coefficient b is defined as:

$$b = 1 - \frac{K_d}{K_s} = \frac{K_d}{H} \tag{24}$$

In undrained conditions, the mass of pore fluid remains constant, which results in a change in volumetric strain and pore pressure through isotropic stress, as follows:

$$d\epsilon_v = \frac{1}{K_u} d\sigma, \quad dp_f = B d\sigma \tag{25}$$

Hereby K_u is the isotropic undrained bulk modulus and B the isotropic Skempton's coefficient $B = \sum B_i/3$ (Skempton 1954). Following the approach of Belmokhtar et al. (2017b), the moduli D_i, U_i and H_i , which describe the anisotropic strain response to isotropic loads, are defined for a drained isotropic compression:

$$D_i = \left(\frac{d\sigma}{d\epsilon_i} \right)_{dp_f=0} \tag{26}$$

for an undrained isotropic compression:

$$U_i = \left(\frac{d\sigma}{d\epsilon_i} \right)_{dm_f=0} \tag{27}$$

and for a pore pressure loading:

$$H_i = - \left(\frac{dp_f}{d\varepsilon_i} \right)_{d\sigma=0} \quad (28)$$

We can also define the anisotropy ratios between deformations in h and in z direction with $R_D = D_h/D_z$, $R_U = U_h/U_z$ and $R_H = H_h/H_z$, which provides:

$$D_h = K_d(2 + R_D), \quad D_z = K_d \left(1 + \frac{2}{R_D} \right) \quad (29)$$

$$H_h = H(2 + R_H), \quad H_z = H \left(1 + \frac{2}{R_H} \right) \quad (30)$$

The undrained moduli U_i are linked to the drained ones with the relationship:

$$\frac{1}{U_i} = \frac{1}{D_i} - B \frac{1}{H_i} \quad (31)$$

One is able to deduce a relationship between the parameters from isotropic and deviatoric experiments:

$$E_z = D_z(1 - 2\nu_{zh}), \quad E_h = \frac{1 - \nu_{hh}}{\frac{1}{D_h} + \frac{\nu_{zh}}{E_z}} \quad (32)$$

Also the parallel and perpendicular Biot's coefficients b_h and b_z can be calculated concurrently (Belmokhtar et al. 2017b):

$$b_h = \frac{\nu_{zh}/H_z + 1/H_h}{\nu_{zh}/D_z + 1/D_h} \quad (33)$$

$$b_z = 2\nu_{zh}b_h + (1 - 2\nu_{zh}) \frac{D_z}{H_z} \quad (34)$$

The bulk Skempton's coefficient B can be determined as:

$$B = \frac{K_u - K_d}{bK_u} \quad (35)$$

and the expression (18) for the two Skempton's coefficients B_z and B_h is simplified to:

$$B_i = \frac{3 \sum_j C_{ij} - \frac{1}{K_s}}{\frac{1}{K_d} - \frac{1}{K_s}} B \quad (36)$$

Note that K_ϕ has to be determined separately in an unjacketed test by measuring the change in pore fluid mass during equal increments of pore pressure and total stress change (e.g. Gassmann 1951; Brown and Korrington 1975; Coussy 2004; Ghabezloo et al. 2008; Makhnenko et al. 2017). This fluid mass change is generally very small for common geomaterials, making the precise measurement a challenging task. For homogeneous materials at the micro-scale, one can

assume $K_\phi = K_s$ (Berryman 1992). If this is not known a priori, it is practical to use some poromechanical relationships for calculating K_ϕ , as given by Ghabezloo et al. (2008), which provide:

$$\frac{1}{K_\phi} = \frac{1}{K_f} - \frac{(1/K_u - 1/K_d + 1/H)}{\phi_0 H (1/K_d - 1/K_u)} \quad (37)$$

The bulk modulus of the pore space K_ϕ can hence be calculated by an experimental evaluation of the undrained bulk modulus K_u , which is less tedious to be determined in an undrained isotropic compression test. The porosity ϕ_0 can be obtained by volume and mass measurements of oven-dried specimens, whereas the bulk modulus of the pore fluid K_f is generally known for a specific fluid, such as for example water. If one is able to measure more than the minimum number of eight independent coefficients (i.e. $E_h, E_z, \nu_{hh}, \nu_{zh}, b_h, b_z, G, K_\phi$, given that ϕ_0 and K_f are known) experimentally, an overdetermined set of parameters is obtained, which can help to check for a compatibility of these values. In this study we did not investigate G , therefore the parameter set which we aimed to characterize contains seven independent coefficients.

3 Materials and Methods

3.1 Specimen Preparation

In this laboratory study we investigated specimens trimmed from COx cores that were extracted at the URL from horizontal boreholes. To preserve the material in its in-situ state as best as possible, that means to avoid desaturation (Ewy 2015) and mechanical damage, cores were shipped and stored in T1 cells, developed by Andra (Conil et al. 2018). Each cell protects an 80 mm diameter COx core, which is wrapped in aluminium foil and a latex membrane to prevent drying. A plastic tube is placed around the core and cement is cast between the membrane and the tube, forming a layer of mechanical protection. This minimises, together with a spring system in axial direction, volume changes of the core.

After receiving the cores, the T1 cells were removed and the cores were immediately covered by a layer of paraffin wax. This protection from drying remained during the following trimming process. Using an air-cooled diamond coring bit, cylinders of 38 mm diameter were trimmed perpendicular and parallel to the bedding plane. The cylinders of 80 mm height were also covered by a paraffin layer, before being cut into cylinders of 76 mm height for triaxial tests or disks of 10 mm height for isotropic tests (Fig. 2), using a diamond wire saw. For protection during storage, the specimens were enveloped by an aluminium foil, covered by a mixture of 70 % paraffin wax and 30 % Vaseline oil.

We carried out a petrophysical characterization, directly after trimming the specimens, and after several months in storage. Table 1 shows the measured characteristics, determined on cuttings of the cores. We obtained the specimen volume through hydrostatic weighting in low-odour hydrocarbon to determine their volume. The dry density was obtained after oven drying at 105 °C. For the porosity calculation, a solid density $\rho_s = 2.69 \text{ g/cm}^3$ (Conil et al. 2018) was assumed. A chilled mirror tensiometer (WP4, Decagon brand) provided measurements of the suction s . The relatively high degree of saturation measured after opening the T1 cells indicates a good drying protection within the cells. In addition, suction and saturation degree were measured on cuttings which were protected and stored in the same way as the specimens. No significant change of these properties was observed during storage, which confirms the effectiveness of the adopted protection methods and a good preservation of the natural water content.

3.2 Isotropic Compression Cell

For the laboratory investigations, we used a high-pressure isotropic thermal compression cell, which is presented in Fig. 3 (Tang et al. 2008; Mohajerani et al. 2012; Belmokhtar et al. 2017a, b; Braun et al. 2019). This cell allows us to test specimens with 38 mm diameter and variable height, placed inside a neoprene membrane in the center of the cell. A silicone heating belt is wrapped around the isotropic cell, which is able to heat up the device. The belt is coupled with a temperature sensor in the vicinity of the specimen, which allows us to maintain a constant cell temperature or impose heating/cooling under constant rates. The cell is filled with silicone oil, which can be set under a pressure of up to 40 MPa by a pressure volume controller (PVC 1, GDS brand). The neoprene membrane isolates the specimen from the silicone oil, so that the pressure of the pore fluid can be controlled independently. The pore pressure is applied from the bottom of the specimen through a porous disk connected to the pressure volume controller PVC 2. During the experiments, we measure the specimen strains locally, using an axial and a radial strain gage (Kyowa brand), glued on the surface of the specimen (Fig. 2).

3.3 Triaxial Compression Cell

A conventional rock mechanics high pressure triaxial cell was used for experiments with deviatoric loading (Fig. 4). A triaxial cell is indispensable for determining the Young moduli and Poisson ratios, necessary for a complete transverse isotropic parameter set. The device used is similar to the isotropic cell, including a pressurized chamber connected to PVC 2, which applies confining pressure to the cylindrical specimen (38 mm diameter, variable height). The specimen, isolated by a neoprene membrane, is submitted to pore pressures through porous stones on its top and bottom surfaces, controlled by PVC 3. Specimen deformations are detected by strain gages attached at specimen mid-height (Fig. 2). The same heating system as in the isotropic cell was used for this device, with a silicone heating belt, connected to an internal thermocouple to regulate the cell temperature. The main difference to the isotropic cell is the auto-compensated piston, which allows us to apply axial deviatoric loads. An auto-compensation chamber pressurized by the confining fluid σ_{rad} (situated in the piston housing, not shown in Fig. 4) keeps the piston in equilibrium, when the pressure applied by PVC 1 is zero. In this case, the specimen is in an isotropic stress state where both axial and radial total stresses are equal ($\sigma_{\text{ax}} = \sigma_{\text{rad}}$). The pressure applied by PVC 1 controls then only the additional deviatoric part of the stress $q = \sigma_{\text{ax}} - \sigma_{\text{rad}}$ (e.g. Fortin et al. 2005).

3.4 Testing Procedure

The COx specimens were mounted in the isotropic and triaxial cells in their initial state at 25 °C. An initial sequence of consolidation, saturation and in-situ stress application was followed, shown schematically in Fig. 5.

First, the specimens were consolidated at constant water content under isotropic stress with a loading rate of 0.1 MPa/min, while the drainage system was kept dry. Most of the specimens were brought to a confining pressure close to the in-situ effective stress between 8 MPa and 10 MPa. Three specimens were brought to a higher confining stress to investigate the effect of confining pressure on swelling strains during the following hydration. An overview of all tested

Table 1 Mean and standard deviation (in parentheses) of petrophysical measurements done on cuttings of three COx cores; with wet and dry density ρ and ρ_d , respectively, porosity ϕ_0 , water content w , saturation degree S_r and suction s

Core	ρ [g/cm ³]	ρ_d [g/cm ³]	ϕ_0 [%]	w [%]	S_r [%]	s [MPa]
EST	2.37	2.22	17.9	7.5	92.5	24.2
53650	(0.00)	(0.01)	(0.2)	(0.1)	(0.8)	(2.1)
EST	2.38	2.21	18.2	7.9	95.3	17.4
57185	(0.00)	(0.00)	(0.2)	(0.1)	(0.7)	(0.1)
EST	2.39	2.22	17.9	7.8	96.3	22.8
58132	(0.02)	(0.02)	(0.6)	(0.2)	(3.6)	(1.3)

Fig. 3 Temperature controlled high pressure isotropic cell, accommodating a rock specimen equipped with strain gages

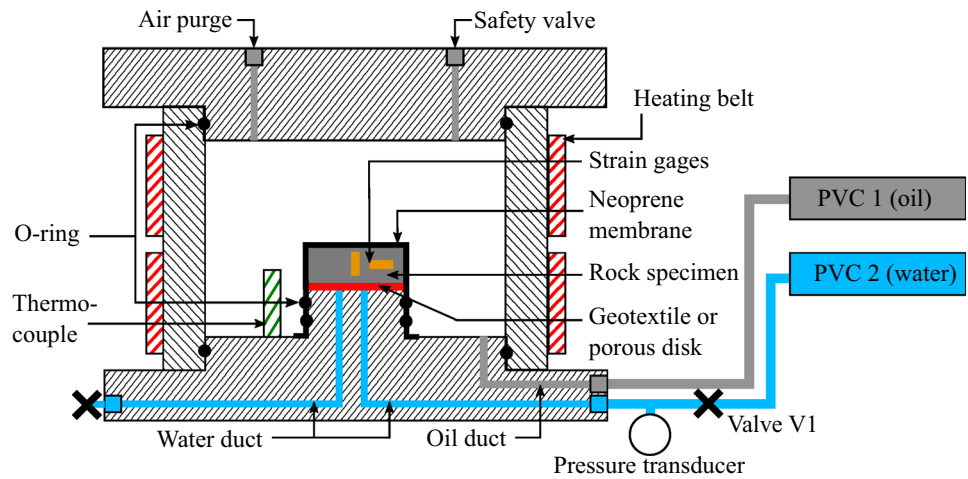
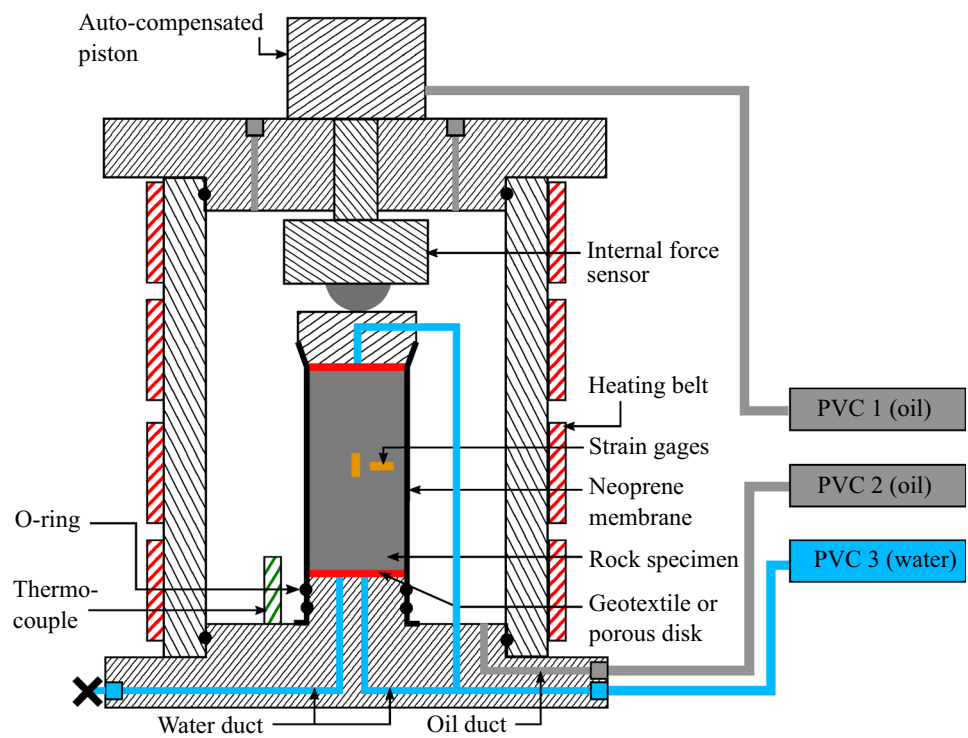


Fig. 4 Temperature controlled high pressure triaxial cell with an auto-compensated load piston and strain gage measuring system



specimens with their respective initial confining stress is given in Table 2.

When specimen deformations remained stable after application of the confining stress, we assume hydraulic equilibrium and a complete dissipation of any generated overpressure in the pores during the loading, similar to the end of secondary consolidation in soils. The air in the dry drainage ducts was evacuated by vacuum for several minutes and the ducts were then filled with synthetic pore water under a pressure of 100 kPa. To prepare synthetic water, salts were added to de-mineralized water according to a recipe provided by Andra, to obtain a fluid composition close to the in-situ one. When injecting pore fluid into a initially partially

unsaturated specimen, we expect a total volume increase composed of (i) the volume changes of an unsaturated medium due to the reduction of suction and the adsorption of water and (ii) the poroelastic response of a saturated medium due to pore pressure increase. The former occurs, when the pore pressure increases from a negative value (corresponding to suction) to zero, while the latter happens under positive pore pressure changes, once the medium is saturated. In order to better distinguish these effects in the experiments, and generate first a predominantly unsaturated response, the initially applied water pressure was chosen relatively small. In this way, we try to limit poroelastic deformations due to pore pressure changes and observe hydration strains only.

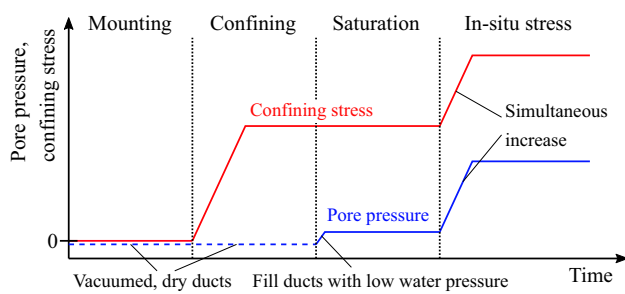


Fig. 5 Mounting and saturation procedure for COx specimens. Specimens are first mounted with dry water-ducts. Vacuum is applied to the ducts in order to evacuate air. The isotropic confining stress is then increased and kept constant. When monitored strains are stable, the water saturation is started with a low back pressure to limit poroelastic strains. After the hydration swelling stabilized, both pore pressure and confining stress are increased simultaneously until the desired stress level close to the in-situ one is reached. Again, strains are monitored and when the deformations are in equilibrium, further testing can be started

A certain positive pressure is however required to fill and saturate the drainage lines of the device. Hydration resulted in swelling strains that stabilized after about five days on all specimens, showing similar transient characteristics. Table 2 lists the measured volumetric swelling strains, which decrease with increasing confining stress (Fig. 6). Here we neglect however possible size effects due to different specimen dimensions and a potentially incomplete saturation at 100 kPa pore pressure.

After hydration, pore pressure and confining pressure were increased simultaneously by 4 MPa under a constant Terzaghi effective stress. The applied pressures were increased until the pore pressure reached 4 MPa.

Consequently, the specimens reached Terzaghi effective stresses, which were equal to the initial confining stress in the saturation phase described in Table 2. We can assume complete saturation when the recorded strains stabilized, indicating hydraulic equilibrium. Rad and Clough (1984) conducted calculations based on Boyle’s and Henry’s laws to estimate the necessary back-pressure for a complete dissolution of the air trapped in pores. They showed that for saturating a specimen which is initially saturated at 90 % and submitted to a vacuum of 80 kPa, one requires around 150 kPa back pressure. Here, while having the same saturation degree and imposed vacuum, we applied a much higher pore pressure of 4 MPa. Favero et al. (2018) carried out tests of the Skempton’s coefficient of initially unsaturated Opalinus clay at different pore pressure levels. For pore pressures higher than 2 MPa, they found that the Skempton’s coefficient remained stable, which indicated complete saturation. Note that during this last saturation phase, no distinction of the measured strains between poroelastic deformations and possible additional swelling (due to further saturation by the increasing back-pressure) could be made.

A step testing procedure, presented by Braun et al. (2019), was then utilized to determine the poroelastic parameters of the material in isotropic tests. This procedure (Fig. 7) consists of increasing or decreasing the confining pressure rapidly at a rate of 0.1 MPa/min and keeping it then constant at a certain level ($\Delta\sigma$). This generates first an undrained response, which permits evaluation of the undrained bulk modulus K_u (Eq. (25)) as a tangent modulus, together with the anisotropic moduli U_h and U_z (Eq. (27)). During a constant load phase, the pore pressures generated in the first phase are allowed to drain by releasing the undrained pore pressure changes through the drainage valve. A drained

Table 2 Overview of tested specimens with their initial saturation phase under stress and their respective subsequent loading paths; the inclined arrows (\searrow, \nearrow) indicate that several load steps were carried out between mentioned effective stresses

Specimen #	Core EST	Saturation phase		Loading path	
		Confining stress [MPa]	Volumetric swelling [%]	Isotropic tests: $\sigma'_{rad} = \sigma'_{ax}$ [MPa]	Deviatoric tests: q [MPa]
ISO1	57185	10	0.71	$10 \searrow 1 \nearrow 18$	-
ISO2	53650	8	0.86	-	-
ISO3	53650	8	0.80	-	-
ISO4	53650	8	0.72	$8 \nearrow 15 \searrow 2$	-
ISO5	53650	10	0.61	$10 \nearrow 36 \searrow 0.5$	-
ISO6	53650	14	0.57	$14 \leftrightarrow 16$	-
ISO7	53650	10	0.66	-	-
ISO8	53650	8	0.95	-	-
ISO9	53650	30	0.15	-	-
ISO10	58132	20	0.33	$20 \leftrightarrow 18$	-
DEV1	57185	10	0.55	$30 \rightarrow 20 \rightarrow 10$	$0 \leftrightarrow 5$ ($@ \sigma'_{rad} = 30/20/10$)
DEV2	57185	10	0.62	-	$0 \leftrightarrow 5$ ($@ \sigma'_{rad} = 11$)
DEV3	57185	20	0.42	-	$0 \leftrightarrow 10$ ($@ \sigma'_{rad} = 10$)

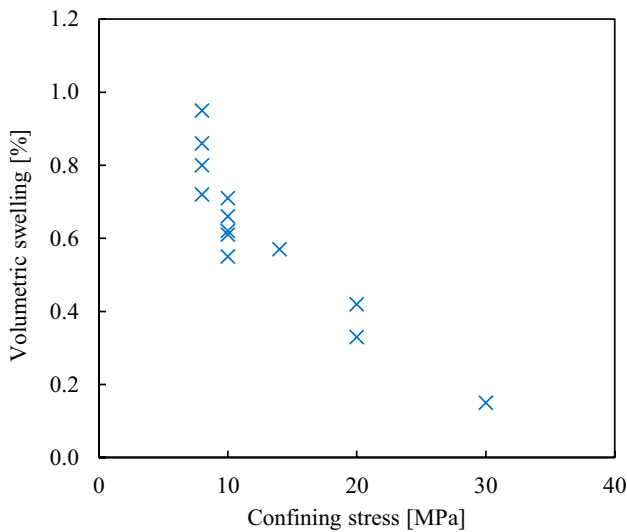


Fig. 6 Measured swelling strains of specimens during hydration under 100 kPa pore pressure and various confining stresses

response can be observed, when all pore pressures have dissipated and the deformations stabilize, providing the drained bulk modulus K_d (Eq. (22)) with D_h and D_z (Eq. (26)). When the confining pressure is held constant and the imposed pore pressure is changed instantly (Δp_f) by the PVC, a transient deformation can be observed. After stabilization of these deformations, the Biot modulus H (Eq. (23)) with H_h and

H_z (Eq. (28)) can be evaluated. This pore pressure loading step can also be carried out independently of a precedent confining pressure loading.

In the deviatoric tests we proceeded similarly to the isotropic loading tests, by applying the deviatoric load q in a relatively rapid loading of 0.1 MPa/min, where we assume undrained conditions. In this phase, we determine the undrained coefficients $E_{u,i}$ and $\nu_{u,i}$ (see also Sec. 2 for the parameter definitions and their evaluation) from the initial slopes of the measurements of stress and strain changes (Fig. 8). Once the target deviatoric stress is reached, we keep it constant, causing a fluid dissipation and equilibration of the pore pressure field inside the specimen. We assume completed drainage when measured strains stabilize. Doing so, we can assure drained conditions before and after each step loading. One can evaluate the drained Young’s moduli and Poisson’s ratios as secant parameters, comparing strains and stresses in the drained states before and after the step. Deviatoric tests on specimens DEV1 and DEV3 were conducted perpendicular to the bedding plane, providing $E_z, \nu_{zh}, E_{u,z}$ and $\nu_{u,zh}$ (compare Fig. 2), whereas the test parallel to the bedding plane on DEV2 provided $E_h, \nu_{hh}, \nu'_{zh}, E_{u,h}, \nu_{u,hh}$ and $\nu'_{u,zh}$.

Undrained conditions during the step increase of q were verified in a single, quick unloading/reloading cycle on specimen DEV2 (Fig. 9). We observe a constant stress-strain slope with no hysteresis after the change of loading direction (Fig. 8a). In parallel, constant slopes indicating constant $\nu_{u,i}$ are observed in Fig. 8b. In a perfectly poroelastic material,

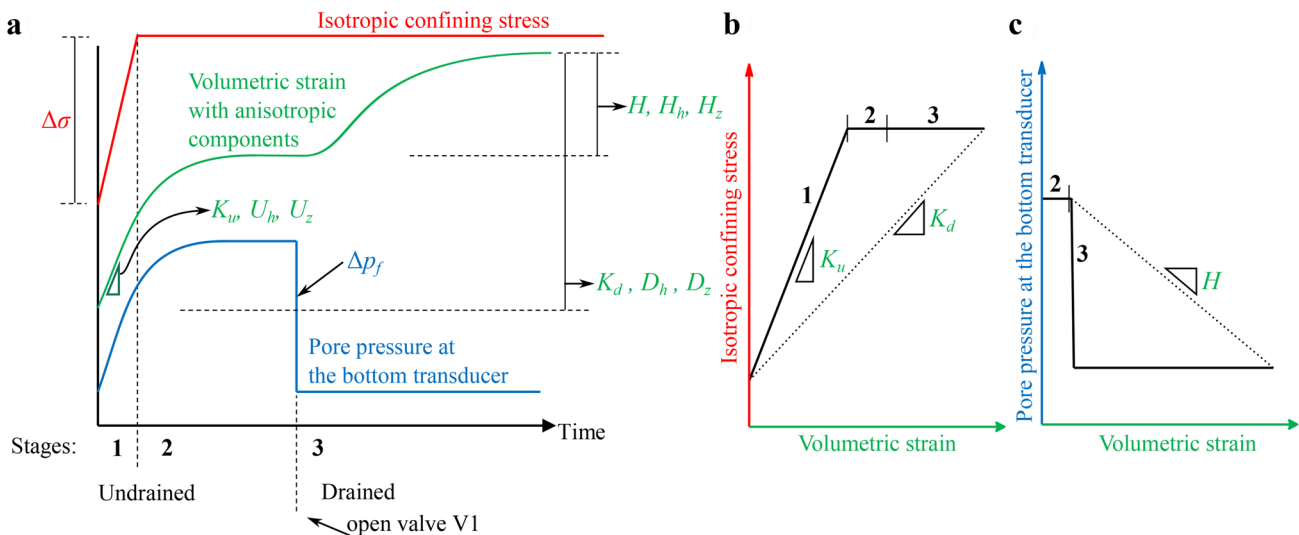


Fig. 7 Schematic representation of the step testing procedure, adopted from Braun et al. (2019) and Hart and Wang (2001). **a** Applied and measured changes of stress, pore pressure and strain with time. A rapid increase of the confining stress $\Delta\sigma$ allows us to measure the undrained properties K_u (Eq. (25)), U_h and U_z (Eq. (27)) from the initial slope of the stress-strain response, shown in b). The drainage system is closed in this phase. After pore pressure and strain

remain constant, the drainage system is opened and a change of pore pressure Δp_f is imposed. This pore pressure change creates a strain response, providing us the (secant) Biot modulus H in c) (see also Eq. (23)), with H_h and H_z (Eq. (28)). The drained parameters K_d (Eq. (22)), D_h and D_z (Eq. (26)) are measured from the secant of the strain response in drained state, before and after the test, as shown in b)

a hysteresis can only appear due to time dependent fluid diffusion processes. If the loading is fast enough, no diffusion occurs, as the specimen remains in constant undrained conditions. In the same test, after the rapid loading (Figs. 8, 9), one can see the additional fluid-dissipation-induced strains with respect to time, as a transient between undrained and drained state.

For isotropic tests ($\sigma' = \sigma'_{ax} = \sigma'_{rad}$), the measured parameters are hereafter presented with respect to the mean between initial and final effective stress applied during each step test, i.e. a parameter measured under a step increase from 4.0 to 6.0 MPa is shown as a data-point at 5.0 MPa. All discussed coefficients were measured under unloading or reloading and are therefore supposed to be elastic. Several subsequent step tests were carried out, starting from the initial stress level and then gradually increasing or decreasing the effective stress in each step with an increment of between 1.0 and 5.0 MPa stress (Fig. 10). These ramps are indicated in Table 2 with inclined arrow symbols (\searrow, \nearrow). Horizontal arrows (\rightarrow) characterise only one step between the indicated effective stresses, which was repeated in the case of a double arrow (\leftrightarrow). The same applies for the deviatoric tests on specimens DEV1 – DEV3. Specimen DEV1 was loaded and unloaded by applying a deviatoric load q between 0 and 5 MPa, which was repeated at effective radial stresses σ'_{rad} of 30, 20 and 10 MPa. Specimens DEV2 and DEV3 were only tested at 11 MPa and 10 MPa effective radial stress, respectively. The resulting parameters are plotted with respect to the average of the initial and final isotropic effective stress σ' at each step loading. Specimens without any loading path given in Table 2 were not tested under hydro-mechanical

experiments. They were either only tested in thermal tests (not discussed here) or had to be abandoned due to technical problems, and are listed only for their data on the swelling upon resaturation.

4 Experimental Results

4.1 Stress Dependent Behaviour Under Isotropic Loading

The conducted isotropic hydromechanical tests provided measurements of the moduli K_d and H with a strong dependency on the effective stress, consistent for all tested specimens (Figs. 11 and 12). Zimmerman et al. (1986) showed, that under the condition of a constant modulus K_s , a stress dependency of the tangent bulk moduli of an isotropic material can be expressed as a function of the Terzaghi mean effective stress. In Sect. 5 we demonstrate, that assuming a constant K_s we are indeed able to reproduce the measured COx properties. As the COx claystone is not isotropic, we decided here to present the following measurements with respect to the Terzaghi isotropic effective stress. The evaluated parameters are later analysed in Sec. 5 as representative functions of the isotropic effective stress.

The moduli K_d and H are smaller than 1.0 GPa for low Terzaghi effective stresses and increase with increasing effective stress (Figs. 11 and 12). With an effective stress larger than around 20 MPa, the moduli appear to remain constant, with values of around 3.0 and 3.5 GPa, respectively. For K_d at effective stresses around 10 MPa, we can observe a

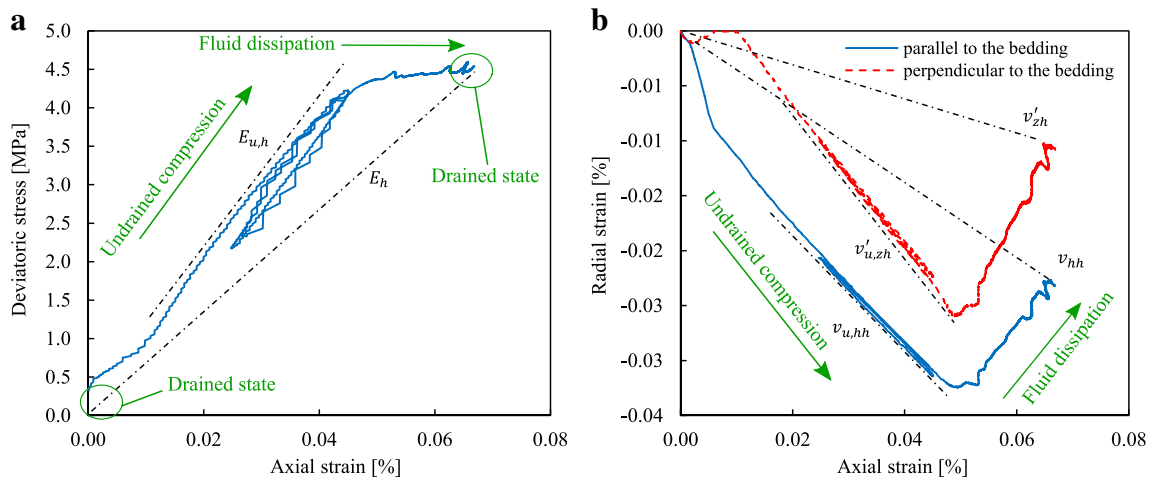


Fig. 8 Measured deformations during a deviatoric test on specimen DEV2 loaded parallel to the bedding plane in (a) function of deviatoric stress q , highlighting the determination of the Young moduli. The fast loading shows a linear undrained response, while pore pressure diffusion induces further compression with time, once the deviatoric stress is held constant. Note that a fast unloading reloading cycle

was only carried out for this specific specimen. No drainage effects in form of a hysteresis were found during the cycle, evidencing a constant undrained condition. (b) Radial strains with respect to axial strains indicating the Poisson ratios, also describing a clear difference between undrained response under fast loading and time dependent fluid dissipation, until reaching drained condition

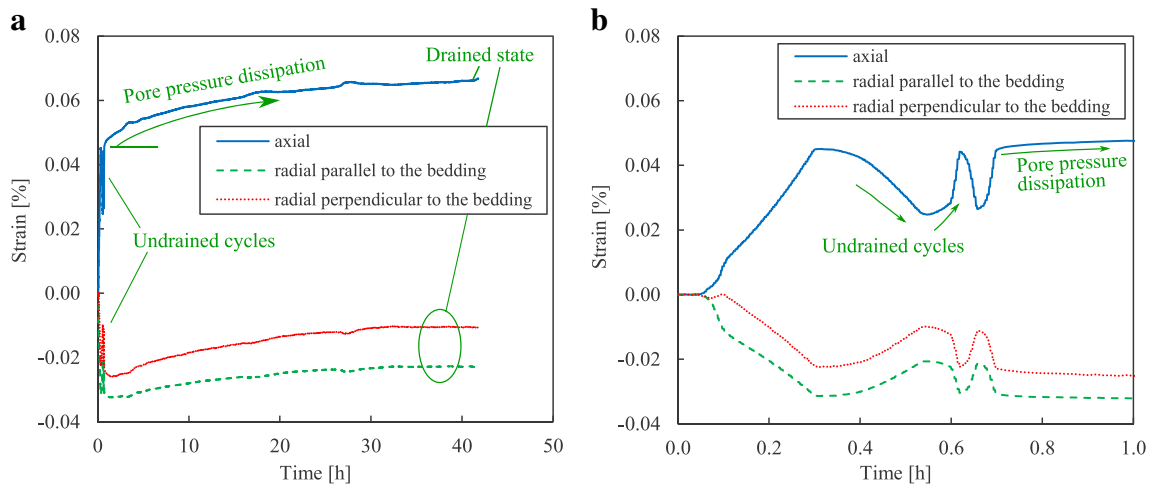


Fig. 9 Measured deformations during a deviatoric test on specimen DEV2 loaded parallel to the bedding plane in (a) function of time, with (b) zoom on the first hour of (a)

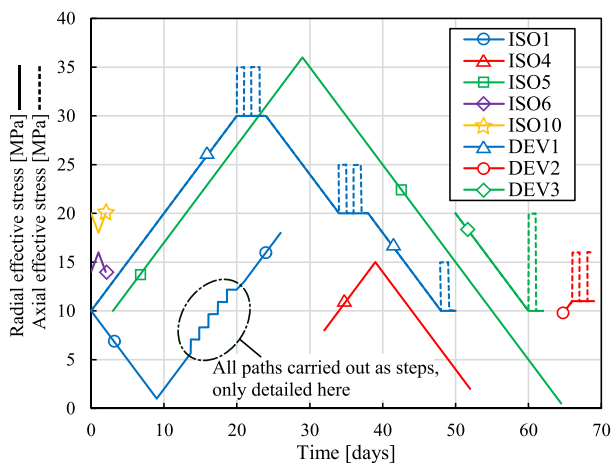


Fig. 10 Schematic representation of the loading paths carried out in this work. The ISO specimens were loaded in steps by changing isotropic confining stress or pore pressure. Note that the inclined lines represent several step loadings, which were not detailed here. Also the DEV specimens were submitted isotropic step loading (solid line), and to additional deviatoric loadings (dashed line) in the form of step-cycles of axial stress. The constant load phase after each isotropic or deviatoric step lasted for at least one day, in order to attain a pore pressure equilibrium. For a better overview, the loading paths were assembled with offsets in the time axis

good agreement with the findings of Mohajerani (2011) and Belmokhtar et al. (2017b). The modulus H was previously measured by Belmokhtar et al. (2017b) at around 10 MPa effective stress with 3.47 and 2.24 GPa, somewhat higher than the present findings.

Interestingly, the reduction of stiffness with effective isotropic stress appears to be reversible, as can be seen in Fig. 13. Here we compare the drained bulk modulus,

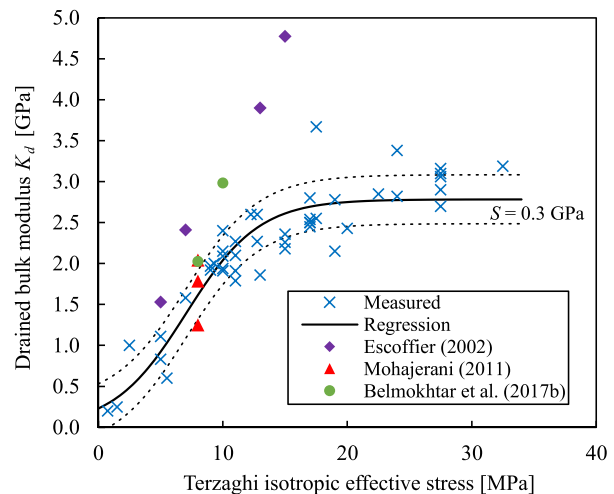


Fig. 11 Measured stress dependent drained bulk modulus K_d compared with a fitted parameter set (Sect. 5). S and dotted lines indicate the standard deviation of the regression

measured on specimen ISO1 after subsequent unloading steps, starting from the initial under-stress-saturated state. The bulk modulus decreases through unloading. After reloading, the drained bulk modulus comes back to the same level as before unloading, comparable also to the values on ISO6 and ISO10, for which the effective stress level was not significantly reduced after saturation.

For the undrained bulk modulus K_u it is difficult to identify a stress dependency (Fig. 14), due to the rather large dispersion of observed values, which was also evidenced in previous studies (Escoffier 2002; Mohajerani 2011; Belmokhtar et al. 2017b).

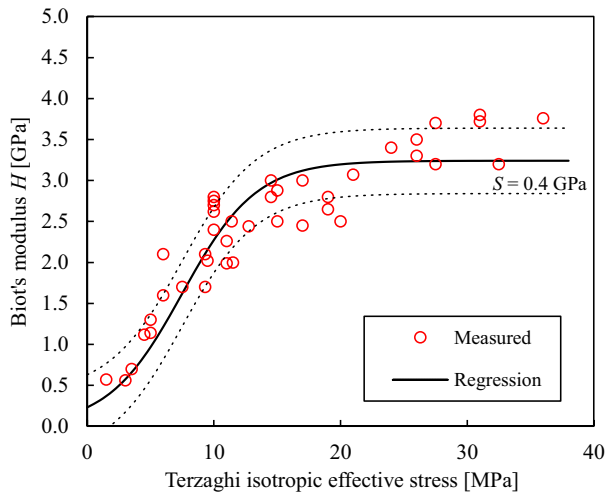


Fig. 12 Measured stress dependent Biot's modulus H compared with a fitted parameter set (Sect. 5). S and dotted lines indicate the standard deviation of the regression

The transversely isotropic strain response was recorded simultaneously with K_d , H and K_u in all tests, resulting in the parameters D_i , H_i and U_i . (Figs. 15, 16 and 17). For drained tests (D_i , H_i) above 20 MPa effective stress, one observes axial strains perpendicular to the bedding plane about three times larger than radial ones. In undrained tests, the ratio of anisotropy varied more significantly with effective stress, with values around 1.5 for low effective stress and values around 2.0 for 30 MPa effective stress. Again, the rather large scatter with some outliers of the measured undrained properties becomes visible on the parameters U_i (Fig. 17).

4.2 Stress Dependent Behaviour Under Deviatoric Loading

In the triaxial tests, we measured E_z and ν_{zh} on specimens DEV1 and DEV3 for effective confining stresses from 10 to 30 MPa (Figs. 18, 19). Whereas the Poisson ratio remained more or less constant with values between 0.10 and 0.17, the Young modulus E_z increased with increasing confining stress from around 3.4 to 6.7 GPa. Compared with the values of E_z from Zhang et al. (2012), Menaceur et al. (2015) and Belmokhtar et al. (2018), a similar stress dependency can be observed. The parameters E_h and ν_{hh} on specimen DEV2 were measured only for 10 MPa isotropic effective stress, with values for E_h between 6.4 and 8.0 GPa and ν_{hh} between 0.30 and 0.34. Note that only two measurements with a relatively large difference were taken for this loading direction.

As expected, the undrained response during triaxial tests produced higher moduli than the drained ones. The parameter $E_{u,z}$ was found between 6.4 and 8.6 GPa and $E_{u,h}$ between 9.8 and 10.8 GPa (Fig. 20). The anisotropy of the undrained

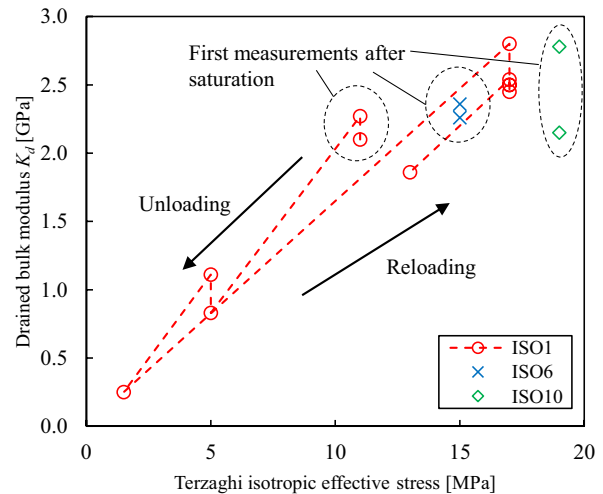


Fig. 13 Measured stress dependent drained bulk modulus K_d on specimens ISO1, ISO6 and ISO10, illustrating the reversible reduction of stiffness with decreasing effective stress

moduli shows a ratio $E_{u,h}/E_{u,z}$ around 1.4, whereas the drained moduli show a ratio E_h/E_z of around 1.8. Interestingly, we can observe relatively large undrained Poisson's ratios, with values higher than 0.35 and a significant scatter (Fig. 21). In contrast to isotropic elastic materials, the Poisson ratios of anisotropic elastic materials have in theory no bounds (Ting and Chen 2005). High Poisson ratios $\nu > 0.5$ have been observed on rocks in the laboratory (e.g. Vutukuri et al. 1974; Hatheway and Kiersch 1982; Islam and Skalle 2013), which can be related to significant anisotropy (Gercek 2007). As for E_h and ν_{hh} , note that only two measurements

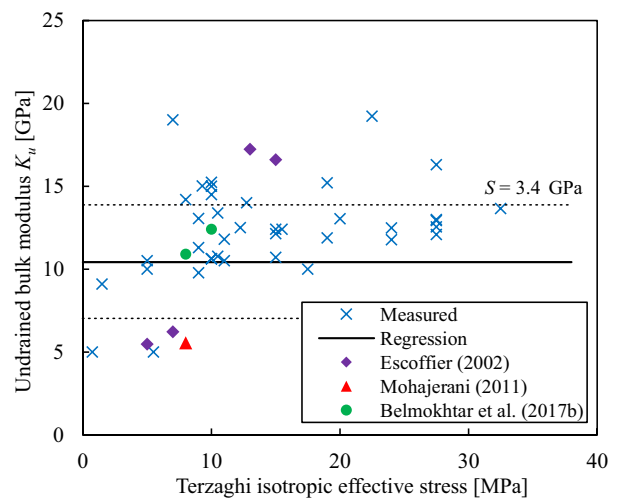


Fig. 14 Measured undrained bulk modulus K_u , compared with a fitted parameter set (Sect. 5). S and dotted lines indicate the standard deviation of the regression

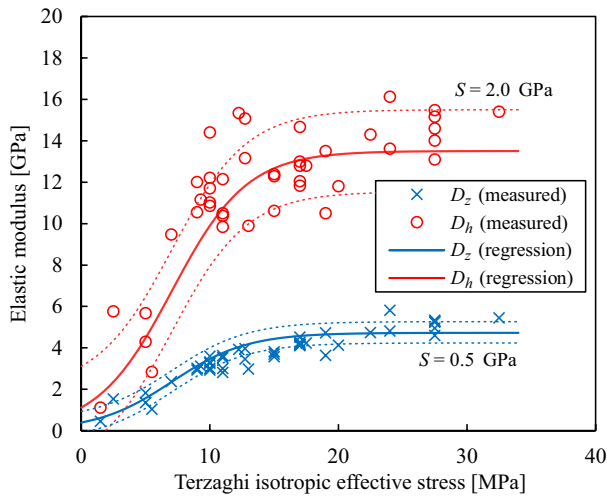


Fig. 15 Measured anisotropic responses D_i during drained compression, compared with a fitted parameter set (Sect. 5). S and dotted lines indicate the standard deviation of the regression

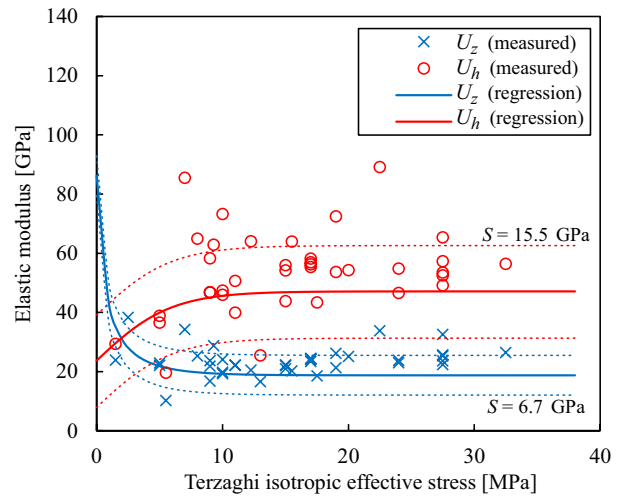


Fig. 17 Measured anisotropic responses U_i during undrained compression, compared with our best-fit parameter set (Sect. 5). S and dotted lines indicate the standard deviation of the regression

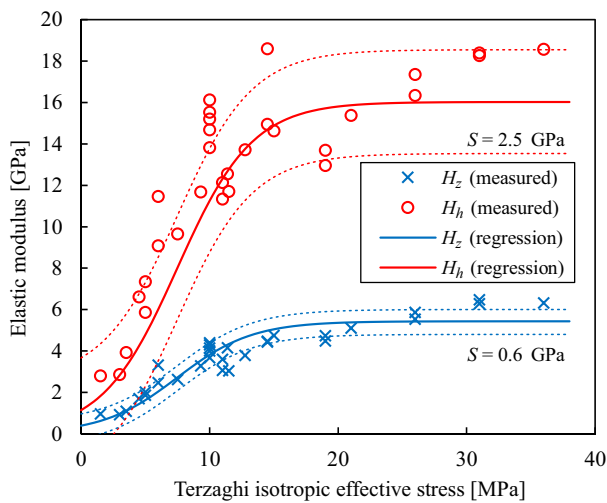


Fig. 16 Measured anisotropic responses H_i during pore pressure tests, compared with a fitted parameter set (Sect. 5). S and dotted lines indicate the standard deviation of the regression

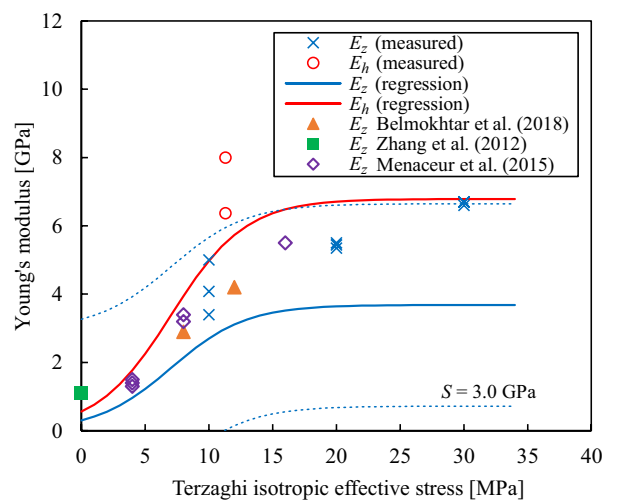


Fig. 18 Measured stress dependent drained Young's modulus E_z perpendicular and E_h parallel to the bedding plane, compared with a fitted parameter set (Sect. 5). S and dotted lines indicate the standard deviation of the regression

have been made for $E_{u,h}$ and $\nu_{u,hh}$, which show a relatively large difference.

5 Regression Analysis

The experimental results evidence an increase of the moduli K_d , D_i , H_z , H_i and E_i with increasing Terzaghi effective stress, starting from a certain value at zero effective stress and reaching a plateau at a given effective stress (e.g. Fig. 11). To describe this trend, we chose an empirical, sigmoid function, used regularly in rock mechanics literature (e.g.

Zimmerman 1991; Hassanzadegan et al. 2014; Ghabezloo 2015). Here we attribute the sigmoid function to E_z :

$$\frac{1}{E_z} = \frac{1}{E_z^\infty} + \left(\frac{1}{E_z^0} - \frac{1}{E_z^\infty} \right) \exp(-\beta\sigma') \tag{38}$$

where E_z increases with the Terzaghi isotropic effective stress σ' from a lower limit E_z^0 to an upper limit E_z^∞ , with the shape of transition governed by a parameter β . In addition, we introduce an anisotropy ratio R_E , which allows us to calculate E_h :

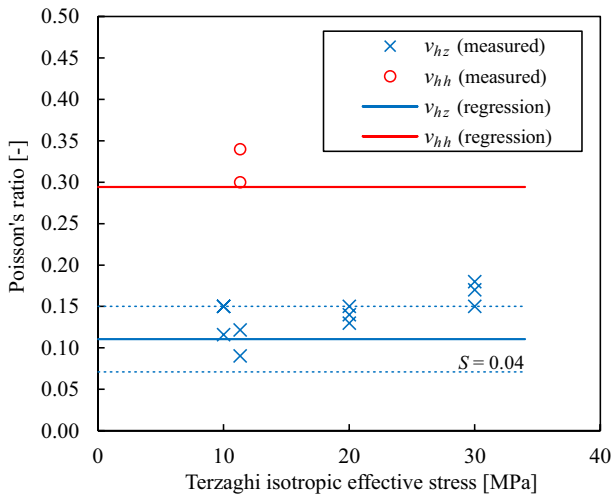


Fig. 19 Measured drained Poisson's ratio v_{zh} perpendicular and v_{hh} parallel to the bedding planes with respect to effective stress, compared with a fitted parameter set (Sect. 5). S and dotted lines indicate the standard deviation of the regression

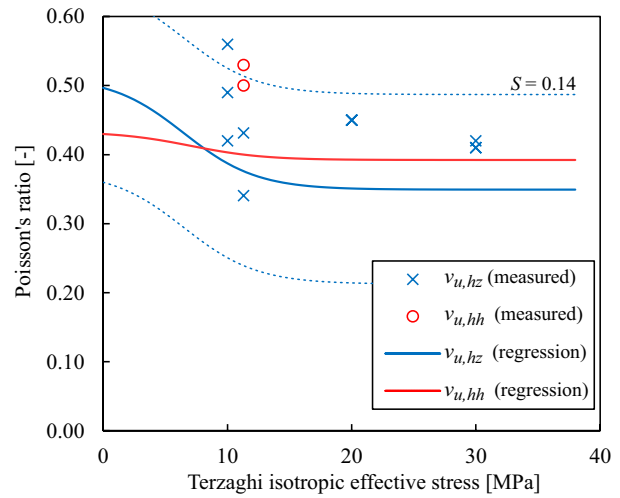


Fig. 21 Measured undrained Poisson's ratio $v_{u,zh}$ perpendicular and $v_{u,hh}$ parallel to the bedding planes with respect to effective stress, compared with a fitted parameter set (Sect. 5). S and dotted lines indicate the standard deviation of the regression

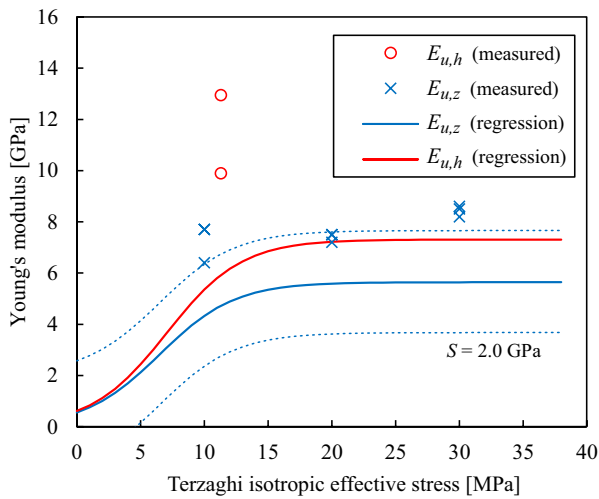


Fig. 20 Measured stress dependent undrained Young's modulus $E_{u,z}$ perpendicular and $E_{u,h}$ parallel to the bedding plane, compared with a fitted parameter set (Sect. 5). S and dotted lines indicate the standard deviation of the regression

$$R_E = E_h/E_z \tag{39}$$

Knowing v_{hz} and v_{hh} , the parameters K_d and D_i can then be evaluated using Eqs. (32) and (29). With Eq. (23), one obtains H by inserting the unjacketed compression modulus K_s . We use then the ratio R_H as another fitting parameter, which provides us H_i (Eq. (23)). The Biot coefficients b_i can now be calculated with Eqs. (33) and (34) and the elastic stiffness matrix M_{ij} by Eqs. (5) – (9).

To evaluate M , one can insert Eq. (37) in Eq. (15), which eliminates K_f and K_ϕ and requires only one additional fitting parameter K_u :

$$\frac{1}{M} = 2(1 - b_h) \left(\frac{b_h(1 - v_{hh})}{E_h} - \frac{b_z v_{hz}}{E_z} \right) + \frac{(1 - b_z)(b_z - 2b_h v_{hz})}{E_z} + \frac{\left(\frac{1}{K_d} - \frac{1}{K_s} \right) \left(\frac{1}{K_u} - \frac{1}{K_s} \right)}{\frac{1}{K_d} - \frac{1}{K_u}} \tag{40}$$

In addition, the properties U_i (Eq. (31)), the undrained elastic stiffness matrix M_{ij}^u (Eq. (20)), its inverse C_{ij}^u and the parameters $E_{u,i}$ and $v_{u,i}$ (Eq. (21)) can be determined. We obtain hence a complete set of parameters depending on the nine unknowns E_z^0 , E_z^∞ , β , R_E , v_{hz} , v_{hh} , R_H , K_s and K_u . Here we assume a priori that the coefficients R_E , R_H , v_{hz} , v_{hh} , K_s and K_u are constant with σ' . Based on these nine coefficients, we can evaluate the theoretical values of the 14 parameters which were investigated in the experiments (D_i , H_i , U_i , E_i , v_i , $E_{u,i}$ and $v_{u,i}$) and compare them to the measured data.

For a given set of nine unknown coefficients, we can compute the sum of the squared relative errors between all our measured data and the calculated dataset. Due to the fact that different parameters with different units were fitted here, we used the method of squared relative errors. To minimize the sum of residuals we used a Python SciPy differential evolution algorithm (Storn and Price 1997; Virtanen et al. 2020), which found a global minimum with the values for the nine unknowns presented in Table 3. The result of the fitting is displayed together with the experimental data in the

respective Figs 11, 12 and 14 – 21. For each curve obtained by the regression, we show its standard deviation S in the Figures.

The data on K_d and H (Figs. 11, 12) show a good fit, with low values of standard deviation (0.3 and 0.4 GPa, respectively). Here the fit gives a high confidence due to the largest number of experimental data. Moreover, the a priori assumption of constant K_s appeared sufficient for reproducing the relationship between the two parameters K_d and H (Eq. (23)). The obtained value of $K_s = 19.69$ GPa is very close to the data provided by Belmokhtar et al. (2017b) of $K_s \approx 21$ GPa. In the case of K_u , we adopted a constant parameter, shown in Fig. 14. Note that due to some significant outliers in the experimental data, the fitted value $K_u = 10.43$ GPa shows a high standard deviation of $S = 3.4$ GPa. Moreover, the fact that the experimental data are not symmetrically distributed around the fitted function indicates a fairly poor fit.

The standard deviation S of the regression for D_h, D_z, H_h and H_z (Figs. 15, 16) was found equal to 2.0, 0.5, 2.5 and 0.6 GPa, respectively. These values indicate acceptable fitting. For the parameters in h direction, S is generally higher due to the higher absolute values. For U_h and U_z , the values of S were notably higher ($S = 15.5$ GPa and 6.7 GPa, respectively), due to the high dispersion of the undrained measurements (Fig. 17).

One can see that the fitted relationships for the deviatoric parameters E_i and ν_i (Figs. 18, 19) simulate qualitatively the measured anisotropic and stress dependent characteristics

of the COx claystone. However, quantitatively we observe a significant underestimation of the measured data, resulting in very large standard deviations S of E_z and ν_{hz} with values of 3.0 GPa and 0.04, respectively. These large standard deviations are also due to the relatively small number of measurements under triaxial stress conditions. For E_h and ν_{hh} , the number of measurements is not sufficient to calculate the standard deviation of the estimate.

Also the obtained relationship for $E_{u,z}$ shows a large standard deviation $S = 1.5$ GPa (Fig. 20). In parallel bedding direction, we measured a much larger $E_{u,h}$ which is cannot be reproduced by the regression. In this direction, the number of measurements is not sufficient for calculating the standard deviation, but we can observe a poor fit in the Figure. In the experiments we measured relatively high undrained Poisson ratios, larger than 0.35 (Fig. 21). Remarkably, the results of the fitted parameter set show similar values, indicating that these high values are compatible with the poroelastic framework. However, the standard deviation of these regressions is rather high ($S = 0.14$ for $\nu_{u,hz}$, no quantitative measure for $\nu_{u,hh}$ due to lack of data-points).

6 Discussion

The proposed multivariate regression scheme is a useful tool to fit multiple dependent variables (experimental material parameters) through multiple independent variables (model

Table 3 Summary of the best-fit parameter set. The independent variables were varied in the fitting procedure. We also present values of other resulting parameters with their stress dependency, which are useful for common numerical applications

	Fit	Resulting parameters in function of σ' [MPa]	
E_z^0	[GPa]	0.30	
E_z^∞	[GPa]	3.68	
β	[MPa ⁻¹]	0.34	
E_z	[GPa]	$[3.06 \exp(-0.34 \sigma') + 0.27]^{-1}$	[Eq. (38)]
R_E	[-]	1.84	
E_h	[GPa]	$1.84 [3.06 \exp(-0.34 \sigma') + 0.27]^{-1}$	[Eq. (39)]
ν_{zh}	[-]	0.11	
ν_{hh}	[-]	0.29	
R_H	[-]	2.95	
K_s	[GPa]	19.69	
b_h	[-]	$[\exp(0.34 \sigma') + 13.02] \cdot [1.18 \exp(0.34 \sigma') + 13.22]^{-1}$	[Eq. (33)]
b_z	[-]	$[\exp(0.34 \sigma') + 13.07] \cdot [1.14 \exp(0.34 \sigma') + 12.93]^{-1}$	[Eq. (34)]
K_u	[GPa]	10.43	
M	[GPa]	$[10.38 \exp(1.02 \sigma') + 2.77 \cdot 10^2 \exp(0.68 \sigma') + 1.79 \cdot 10^3 \exp(0.34 \sigma')]$ $\times [\exp(1.02 \sigma') + 0.26 \cdot 10^2 \exp(0.68 \sigma') + 1.71 \cdot 10^2 \exp(0.34 \sigma') - 1.89]^{-1}$	[Eq. (40)]

parameters) and to analyse a complex set of transversely isotropic poroelastic parameters. For properties measured under isotropic loading conditions, the model shows a good fit due to the large number of experimental data. Some compatibility issues were encountered in the response to deviatoric loads, where the model significantly underestimates the measured moduli E_i and $E_{u,i}$. This could be due to the fact that we express the moduli only as a function of effective isotropic stress, which is not sufficient for reproducing the observed behaviour in deviatoric tests. Some studies (e.g. Cariou et al. 2012; Zhang et al. 2019) reported an increase of the Young modulus as a function of q during tests under partially saturated conditions. Additional experimental results and the consideration of a parameter dependency on q could improve the set of material coefficients.

We are also able to evaluate several other poroelastic characteristics, not measured experimentally, by using the fitted dataset. For instance, we can calculate the Biot modulus M through Eq. (40), presented in Fig. 22 and Table 3. This coefficient, often used as a model parameter in engineering applications, changes very little with effective stress and is close to the undrained bulk modulus K_u .

The Biot coefficients b_h and b_z were calculated using Eqs. (33) and (34). One can compute stress dependent Biot's coefficients, presented in Fig. 23 and Table 3. Both coefficients show values close to 1.0 for low effective stress, decrease slightly with effective stress and remain constant above around 14 MPa effective stress. At the in-situ effective stress of around 10 MPa, we obtain values b_i close to 0.9, which is agreement with previous studies (Fig. 23). Interestingly, a less pronounced anisotropy can be seen here, compared to other elastic coefficients. High values of b_i originate from small differences between K_d and H , while a small anisotropy is due to small differences between D_h and H_h , and between D_z and H_z .

The isotropic Skempton's coefficient B (Fig. 24), calculated through Eq. (35), shows relatively high values between 0.9 and 1.0. Similar to b_i , this coefficient decreases slightly with effective stress up to 14 MPa. Also Belmokhtar et al. (2017b) and Mohajerani et al. (2012, 2014) determined rather high coefficients B with values of 0.87 and 0.84, respectively. Using Eq. (36), one is able to calculate the anisotropic Skempton's coefficients, presented in Fig. 24. Note that here, as well as for b_i , a combination of different involved regressions increases the uncertainty of the calculated relationships. One observes a large difference between B_z and B_h , with values of 1.6 and 0.5, respectively, at 10 MPa Terzaghi effective stress. Such significant anisotropies of the Skempton's coefficient have been addressed by Holt et al. (2018), who tested soft shales with B close to 1.0. They found properties equivalent to B_z around 1.5 and B_h around 0.6, similar to the findings of this study. These authors were able to back-calculate their measurements by

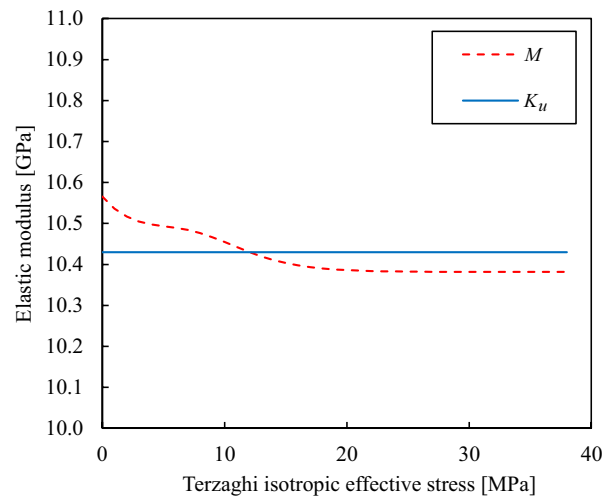


Fig. 22 Biot's modulus M compared with the undrained bulk modulus K_u , both evaluated through the regression analysis

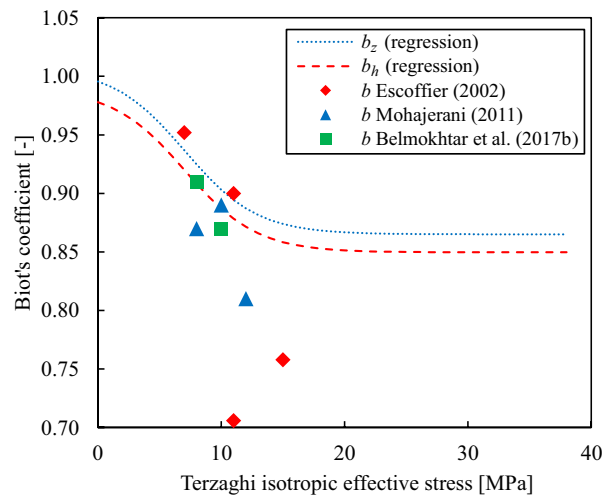


Fig. 23 Biot's effective stress coefficients b_i obtained through the regression, compared with literature data on the isotropic parameter b . Two datapoints from Escoffier (2002) for $b = 0.54$ and 0.32 , both at 23 MPa effective stress, are not shown in the figure

adopting a transversely isotropic poroelastic model. Moreover, they emphasized the significance of anisotropic B_i on pore pressure increase due to subsurface drilling, injection or depletion. In the numerical study of Guayacán-Carrillo et al. (2017), transversely isotropic material parameters provided the best results to model the in-situ measurements of induced pore pressures during excavation of galleries in the COx claystone. Although not discussed explicitly, the material properties used in their study most likely resulted in anisotropic Skempton's parameters, able to reproduce the non-uniform pore pressure field observed around the galleries.

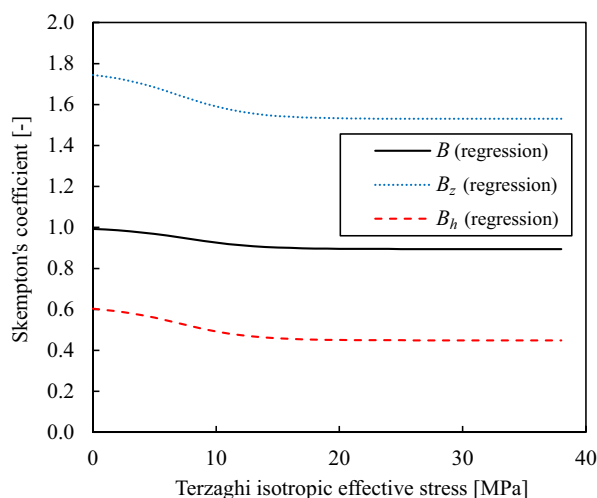


Fig. 24 Skempton's coefficients B and B_i evaluated through our regression analysis

7 Conclusion

A laboratory study using experimental equipment and testing procedures adopted for very low permeability materials allowed us to conduct a series of time efficient isotropic and deviatoric experiments on the COx claystone. Precise strain gage measurements were employed to investigate its transversely isotropic poromechanical properties and to establish a set of independent poroelastic parameters.

- Tests on different specimens from three cores provided consistent poromechanical coefficients, which confirms the reproducibility of the experiments, the same specimen qualities and shows no noticeable natural variability between the cores.
- The measurements show a clear stress dependency of the drained bulk modulus K_d and the Biot modulus H , the drained and undrained Young moduli and a less pronounced stress dependency of the undrained bulk modulus and the undrained Young modulus. The drained and undrained Poisson ratios perpendicular to the isotropy plane were observed to change very little with effective stress.
- The decrease of the drained bulk modulus with decreasing effective stress was observed to be reversible in isotropic tests. The reduction of moduli could probably be attributed to an elastic opening of microcracks.
- A remarkable anisotropy was found for several elastic coefficients. The drained Young moduli showed an anisotropy ratio close to 1.8, while the isotropic stress parameters D_i and H_i had a ratio close to 3.0 (ratio between modulus parallel and perpendicular to bedding). Drained Poisson's ratios were close to 0.3 parallel to bedding,

whereas perpendicular to bedding we found values around 0.15. In undrained conditions, the anisotropy of moduli was less developed. Relatively high undrained Poisson's ratios around 0.4 illustrate peculiar undrained characteristics.

- We carried out a regression analysis, which aimed to match a stress dependent set of transversely isotropic poroelastic coefficients to the laboratory measurements. The obtained seven independent coefficients (9 coefficients due to stress dependency, Table 3) could satisfactorily represent the measured parameters under isotropic loading conditions. Some compatibility issues were encountered, where elastic properties evaluated from deviatoric tests tend to be stiffer than those back-calculated from the fitted parameter set.
- The observed poor fit for parameters measured under deviatoric loading conditions could be improved by additional experimental data, by taking into account a parameter dependency on deviatoric stress or considering other effects, which are not captured by our transversely isotropic poroelasticity assumption with parameters depending on isotropic stress only.
- The fittedunjacketed compression modulus, which is assumed to be isotropic at the micro-scale and constant with effective confining stress, gave a value of $K_s = 19.69$ GPa. This is in accordance with the direct measurements of Belmokhtar et al. (2017b).
- A negligible anisotropy of the calculated Biot's coefficients b_h and b_z was indicated by the fitted parameters. Relatively high values of the Biot coefficients highlight the importance of hydromechanical couplings in this material. The calculated Skempton's coefficients showed a significant anisotropy, with higher values perpendicular to bedding.

The precise knowledge of the poromechanical properties of the COx claystone is important not only for the hydro-mechanical modelling of the rock behaviour around excavated drifts (Guayacán-Carrillo et al. 2017), but also for the analysis of the deformations due to thermally induced pore pressures (Gens et al. 2007; Garitte et al. 2017). The parameters evaluated in this study give confidence due to their inter-compatibility, evidencing a clear anisotropy. The observed stress dependency of elastic properties could be considered in in-situ modelling. The material was seen to become more compliant under decreasing effective stresses, which increases the elastic deformations in unloading paths.

Compliance with Ethical Standards

Conflict of interest The authors declare that there are no known conflicts of interest associated with this publication.

References

- Aichi M, Tokunaga T (2012) Material coefficients of multiphase thermoporoelasticity for anisotropic micro-heterogeneous porous media. *Int J Solids Struct* 49(23–24):3388–3396
- Andra (2005) Dossier 2005 Argile: Evaluation of the feasibility of a geological repository in an argillaceous formation. URL [https://international.andra.fr/sites/international/files/2019-03/3-Dossier 2005 Argile Synthesis - Evaluation of the feasibility of a geological repository in an argillaceous formation_0.pdf](https://international.andra.fr/sites/international/files/2019-03/3-Dossier%2005%20Argile%20Synthesis%20-%20Evaluation%20of%20the%20feasibility%20of%20a%20geological%20repository%20in%20an%20argillaceous%20formation_0.pdf)
- Belmokhtar M, Delage P, Ghabezloo S, Conil N (2017a) Thermal volume changes and creep in the callovo-Oxfordian claystone. *Rock Mech Rock Eng* 50(9):2297–2309
- Belmokhtar M, Delage P, Ghabezloo S, Tang AM, Menaceur H, Conil N (2017b) Poroelasticity of the Callovo-Oxfordian claystone. *Rock Mech Rock Eng* 50(4):871–889
- Belmokhtar M, Delage P, Ghabezloo S, Conil N (2018) Drained Triaxial Tests in Low-Permeability Shales: Application to the Callovo-Oxfordian Claystone. *Rock Mech Rock Eng* 51(7):1979–1993
- Berryman JG (1992) Effective stress for transport properties of inhomogeneous porous rock. *J Geophys Res* 97(B12):17409–17424
- Biot MA, Willis DG (1957) The elastic coefficients of the theory of consolidation. *J Appl Mech* 24:594–601
- Braun P, Ghabezloo S, Delage P, Sulem J, Conil N (2019) Determination of multiple thermo-hydro-mechanical rock properties in a single transient experiment: application to shales. *Rock Mech Rock Eng* 52(7):2023–2038
- Braun P, Ghabezloo S, Delage P, Sulem J, Conil N (2020) Thermo-poro-elastic behaviour of a transversely isotropic shale: Thermal expansion and pressurization, (Submitted)
- Brown RJS, Korrington J (1975) On the dependence of the elastic properties of a porous rock on the compressibility of the pore fluid. *Geophysics* 40(4):608–616
- Cariou S, Duan Z, Davy C, Skoczylas F, Dormieux L (2012) Poromechanics of partially saturated CO_x argillite. *Appl Clay Sci* 56:36–47
- Cheng AHD (1997) Material coefficients of anisotropic poroelasticity. *Int J Rock Mech Mining Sci* 34(2):199–205
- Chiarelli AS (2000) Étude expérimentale et modélisation du comportement mécanique de l'argilite de l'Est, Influence de la profondeur et de la teneur en eau. PhD thesis, Université Lille I
- Conil N, Talandier J, Djizanne H, de La Vaissière R, Righini-Waz C, Auvray C, Morlot C, Armand G (2018) How rock samples can be representative of in situ condition: A case study of Callovo-Oxfordian claystones. *J Rock Mech Geotechn Eng* 10(4):613–623
- Coussy O (2004) *Poromechanics*. J. Wiley & Sons, New York
- Escoffier S (2002) Caractérisation expérimentale du comportement hydromécanique des argilites de Meuse/Haute-Marne. PhD thesis, Institut National Polytechnique de Lorraine
- Ewy RT (2015) Shale/claystone response to air and liquid exposure, and implications for handling, sampling and testing. *Int J Rock Mech Mining Sci* 80:388–401
- Favero V, Ferrari A, Laloui L (2018) Anisotropic behaviour of opalinus clay through consolidated and drained triaxial testing in saturated conditions. *Rock Mech Rock Eng* 51(5):1305–1319
- Fortin J, Schubnel A, Guéguen Y (2005) Elastic wave velocities and permeability evolution during compaction of bleurswiller sandstone. *Int J Rock Mech Mining Sci* 42(7):873–889
- Garitte B, Nguyen TS, Barnichon JD, Graupner BJ, Lee C, Maekawa K, Manepally C, Ofoegbu G, Dasgupta B, Fedors R, Pan PZ, Feng XT, Rutqvist J, Chen F, Birkholzer J, Wang Q, Kolditz O, Shao H (2017) Modelling the Mont Terri HE-D experiment for the Thermal-Hydraulic-Mechanical response of a bedded argillaceous formation to heating. *Environm Earth Sci* 76(9):1–20
- Gassmann F (1951) Über die Elastizität poröser Medien. *Vierteljahrsschrift der Naturforschenden Gesellschaft in Zürich* 96(1–51):1–21
- Gens A, Vaunat J, Garitte B, Wileveau Y (2007) In situ behaviour of a stiff layered clay subject to thermal loading: observations and interpretation. *Géotechnique* 57(2):207–228
- Gercek H (2007) Poisson's ratio values for rocks. *Int J Rock Mech Mining Sci* 44(1):1–13. <https://doi.org/10.1016/j.ijrmms.2006.04.011>
- Ghabezloo S (2015) A micromechanical model for the effective compressibility of sandstones. *Eur J Mech A Sol* 51:140–153
- Ghabezloo S, Sulem J, Guédon S, Martineau F, Saint-Marc J (2008) Poromechanical behaviour of hardened cement paste under isotropic loading. *Cement Concrete Res Research* 38:1424–1437
- Guayacán-Carrillo LM, Ghabezloo S, Sulem J, Seyedi DM, Armand G (2017) Effect of anisotropy and hydro-mechanical couplings on pore pressure evolution during tunnel excavation in low-permeability ground. *Int J Rock Mech Mining Sci* 97:1–14
- Hart DJ, Wang HF (2001) A single test method for determination of poroelastic constants and flow parameters in rocks with low hydraulic conductivities. *Int J Rock Mech Mining Sci* 38(4):577–583
- Hassanzadegan A, Blöcher G, Milsch H, Urpi L, Zimmermann G (2014) The effects of temperature and pressure on the porosity evolution of flechtinger sandstone. *Rock Mech Rock Eng* 47(2):421–434
- Hatheway AW, Kiersch GA (1982) Engineering properties of rock. In: Carmichael RS (ed) *Handbook of Physical Properties of Rocks*. CRC Press, Boca Raton FL, pp 289–331
- Holt RM, Bakk A, Stenebraten JF, Bauer A, Fjaer E (2018) Skempton's A - A key to man-induced subsurface pore pressure changes. In: 52nd U.S. Rock Mechanics/Geomechanics Symposium, American Rock Mechanics Association, Seattle
- Islam MA, Skalle P (2013) An experimental investigation of shale mechanical properties through drained and undrained test mechanisms. *Rock Mech Rock Eng* 46(6):1391–1413
- Makhnenko RY, Tarokh A, Podladchikov YY (2017) On the Unjacketed Moduli of Sedimentary Rock. In: Vandamme M, Dangla P, Pereira JM, Ghabezloo S (eds) *Poromechanics VI - Proceedings of the 6th Biot Conference on Poromechanics*, American Society of Civil Engineers, pp 897–904
- Menaceur H, Delage P, Am Tang, Conil N (2015) The thermo-mechanical behaviour of the Callovo-Oxfordian claystone. *Int J Rock Mech Mining Sci* 78:290–303
- Mohajerani M (2011) Etude expérimentale du comportement thermo-hydro-mécanique de l'argilite du Callovo-Oxfordien. PhD thesis, Université Paris-Est
- Mohajerani M, Delage P, Sulem J, Monfared M, Tang AM, Gatmiri B (2012) A laboratory investigation of thermally induced pore pressures in the Callovo-Oxfordian claystone. *Int J Rock Mech Mining Sci* 52:112–121
- Mohajerani M, Delage P, Sulem J, Monfared M, Tang AM, Gatmiri B (2014) The thermal volume changes of the Callovo-Oxfordian claystone. *Rock Mech Rock Eng* 47(1):131–142
- Popov VL, Heß M, Willert E (2019) *Transversely Isotropic Problems*. Springer, Berlin, pp 205–212
- Rad NS, Clough GW (1984) New procedure for saturating sand specimens. *J Geotechn Eng* 110(9):1205–1218
- Schmitt L, Forsans T, Santarelli F (1994) Shale testing and capillary phenomena. *Int J Rock Mech Mining Sci Geomech Abstracts* 31(5):411–427
- Skempton AW (1954) The Pore-Pressure Coefficients A and B. *Géotechnique* 4(4):143–147
- Storn R, Price K (1997) Differential evolution—a simple and efficient heuristic for global optimization over continuous spaces. *J Global Optimiz* 11(4):341–359
- Tang AM, Cui YJ, Barnel N (2008) Thermo-mechanical behaviour of a compacted swelling clay. *Géotechnique* 58(1):45–54

- Ting TC, Chen T (2005) Poisson's ratio for anisotropic elastic materials can have no bounds. *Quarterly J Mech Appl Math* 58(1):73–82
- Virtanen P, Gommers R, Oliphant TE, Haberland M, Reddy T, Cournapeau D, Burovski E, Peterson P, Weckesser W, Bright J, van der Walt SJ, Brett M, Wilson J, Jarrod Millman K, Mayorov N, Nelson ARJ, Jones E, Kern R, Larson E, Carey C, Polat I, Feng Y, Moore EW, VanderPlas J, Laxalde D, Perktold J, Cimrman R, Henriksen I, Quintero EA, Harris CR, Archibald AM, Ribeiro AH, Pedregosa F, van Mulbregt P, SciPy 1.0 Contributors, (2020) SciPy 1.0: Fundamental Algorithms for Scientific Computing in Python. *Nature Methods* 17:261–272. <https://doi.org/10.1038/s41592-019-0686-2>, (in press)
- Vutukuri VS, Lama RD, Saluja SS (1974) Handbook on mechanical properties of rocks. Trans Tech Publications, Clausthal
- Wileveau Y, Cornet FH, Desroches J, Blumling P (2007) Complete in situ stress determination in an argillite sedimentary formation. *Phys Chem Earth* 32(8–14):866–878
- Zhang CL, Armand G, Conil N, Laurich B (2019) Investigation on anisotropy of mechanical properties of Callovo-Oxfordian claystone. *Eng Geol* 251:128–145
- Zhang F, Xie SY, Hu DW, Shao JF, Gatmiri B (2012) Effect of water content and structural anisotropy on mechanical property of claystone. *Appl Clay Sci* 69:79–86
- Zimmerman RW (1991) Compressibility of sandstones. Elsevier Sci, Amsterdam
- Zimmerman W, Somerton WH, King MS (1986) Compressibility of Porous Rocks. *J Geophys Res* 91(B12):12765–12777

Publisher's Note Springer Nature remains neutral with regard to jurisdictional claims in published maps and institutional affiliations.